XXIV Biennial Symposium on Measuring Techniques in Turbomachinery
Prague, Czech Republic, 29 - 31 August 2018
Paper No MTT2418B45

MEASUREMENTS OF FLOW STRUCTURES IN A TURBINE CASCADE USING A SPIV

Y.Tian, H. Ma

National Key Laboratory of Science and Technology on Aero-Engines Collaborative Innovation Center of Advanced Aero-Engine Beihang University, Beijing, China

Keywords: turbine cascade, stereoscopic PIV, secondary flow, tip leakage

ABSTRACT

This paper presents the application of the stereoscopic particle-image velocimetry (SPIV) in a Low-speed Turbine Cascade. In the measurements, a pair of frame-straddling-based CCD cameras was configured at different sides of the laser light sheet, and the appropriate tracing particles were used. It is demonstrated that the measured flow field with such a configuration are very important for the investigations of unsteady flow structures of the tip leakage vortex (TLV) and secondary flows inside the turbine cascade. And this configuration is also easy to use in turbine cascade. The instantaneous snapshots, time-averaged flow field and statistic flow field inside the turbine cascade passage were obtained. The representative flow structures, such as the TLV, the passage vortex and the induced vortex, can also be depicted clearly. Moreover, according to this investigation, some useful proposals are presented for the application of SPIV in the turbine cascade.

NOMENCLATURE

C	chord (mm)
Cx	axial chord (mm)
Cvs	streamwise velocity coefficient
Re	Reynolds number
Tu	turbulence intensity
τ	solidity
w	vorticity
β	flow angle
k	kinetic energy

INTRODUCTION

The flow structures inside the turbine passage are three-dimensionally, and highly unsteady. Therefore, many flow mechanisms are still unclear and needed to make a deep exploration depending on the improvement of measurement methods. In the past several decades, numerous experimental investigations for flows in turbomachinery have been performed by using a series of measurement techniques, such as aero-probe, fast-response pressure probe, HWA, LDV and L2F [1][2][3][4][5][6]. However, they are all point-based measurement techniques and have no capability to capture the unsteady flow structures in turbomachinery. In contrast, particle-image velocimetry (PIV) makes the measurement of instantaneous velocity field possible, and enables the investigation of the unsteady spatial structures typically encountered in turbomachinery.

In the previous investigations, the PIV has been used for the flow field measurements in turbomachines by Bryanston-Cross et al. [7] and Wernet [8]. Ni [9] performed the PIV measurements on a turbine cascade. But these are all the measurements of blade-to-blade. In order to investigate the flow structures in the hub-to-tip plane, the Stereoscopic Particle-image Velocity (SPIV) was employed by Lang [10] and Wernet [11]. In our group, the experimental study using SPIV was conducted in an axial compressor [12]. Some special flow structures were found.

In view of the superiorities of SPIV [12][13] and rare investigations of turbines, a SPIV measurement was conducted on a Low-Speed Turbine Cascade. The corresponding investigations of aerodynamic performance have been done using the five-hole probe [14]. In this paper, it is aimed at the study of specific flow phenomena inside the turbine passage and identifying the flow mechanism, which can contribute to the further design and the improvement of the performance of the turbines.

EXPERIMENTAL APPARATUS

In this investigation, the measurements were performed on a Low-Speed Wind Tunnel driven by a centrifugal blower in Beihang University. The experimental facility was operated using turbine cascade with the incidence angle of 0 degree and the exit Reynolds number of 1.7×10^5 based on the blade chord. The mainstream turbulence levels of inlet flow are given 4%.

As for the linear turbine cascade, it is composed of five turbine blades, two lateral plates and two tail boards. The turbine blades are made of aluminum and mounted to the bottom lateral plate. Fig.1 shows the overall view of Wind Tunnel. All the measurements are conducted on the third blade. The two tailboards are used to adjust the periodicity of the airflow. And more detailed

cascade properties are summarized in table 1. During the experiments, all the solid surfaces of the linear turbine cascade are covered with the black wallpapers except for the transparent optical glass.

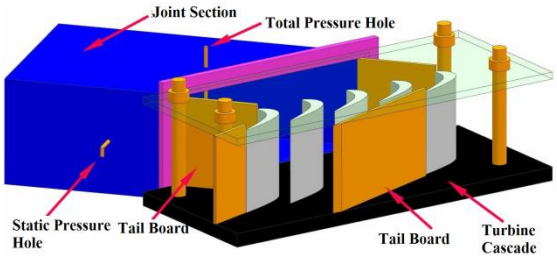

Figure 1: Overall view of the Low-Speed Wind Tunnel

Table 1: Design parameters of linear turbine cascade

Number of blades	N	5
Chord	C	102mm
Axial chord	Cx	71mm
Tip clearance	%C	1.18
Solidity	τ	1.36
Inlet flow angle	β1	33.6°
Outlet flow angle	B2	67°
Exit Reynolds number	Re	1.7×10^5

EXPERIMENTAL SETUP OF SPIV SYSTEM

SPIV System and Light Sheet Delivery

A PIV system, developed by MicroVec Incorporation, was employed in this experiment. Fig. 2 presents the schematic diagram of the SPIV configuration. The laser source is a double cavity Nd: YAG laser with the maximum illumination energy of 200 mJ /pulse at a repetition rate of 15 Hz. As shown in the figure, the CCD cameras with the resolution of 2048×2048 (4M) were configured at different sides of laser sheet which meets the Scheimpflüg condition. The macro lens was also used. Two cameras and the laser arm were all fixed on the same mounting base which was mounted on the same three-freedom displacement mechanism.

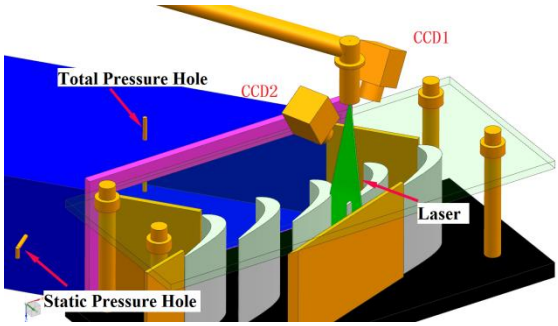

Figure 2: Schematic diagram of the SPIV configuration

Seeding and Calibration

The measured flow field of PIV experiments is largely determined by the properties of the tracer particles. In general, the tracer particles not only satisfy non-toxic, non-corrosive, and non-environmental pollution to the human body, but also satisfy the requirements of flow mobility, light scattering, and chemical stability. In this experiment, diisooctyl sebacate (DEHS) was used as the tracer particle for SPIV measurement, which is non-toxic, non-polluting, and has good light scattering properties. The oil is atomized by a high pressure atomizing nozzle in the particle generator to break it into liquid particles. The diameter of the broken particles is about 1 um, which has good follow mobility and the particle distribution is also ideal.

A thin pipe with the same diameter at the outlet of the particle generator was used for particle spraying to achieve the effect of diversion. And it can also achieve the effect of uniform tracer particles. In this experiment, the spraying position was located at the upstream of the expansion section of the wind tunnel. The wake generated by the air flow through the thin tube was completely dissipated after passing through the honeycomb and the two-layer gauze structure, and the influence on the flow field of the turbine cascade channel was negligible.

The calibration of optical system must be performed to correct the perspective distortion caused by the inclined view of the illuminated light sheet plane and the differences in optical system magnification between the CCD cameras. The calibration target is a 50mm×50mm×6mm (length × width × thickness) black plate with 2 mm diameter calibration dots, as can be seen from the Fig.3. During the calibration, nine dots arranged as the Sudoku was applied to calibrate the view. Particle analysis, image correction and grid establishment were then conducted. Finally, the 3-D calibration was automatically executed by the MicroVec software. In order to make sure that the calibration function is trustworthy, the misregistration of the two viewing directions was assessed [15][16]. As shown, it can be known that the maximum displacement is 0.108743mm which corresponds to the mismatch less than 2.7 pixels. The employment of macro lens may be one important reason for the disparity.

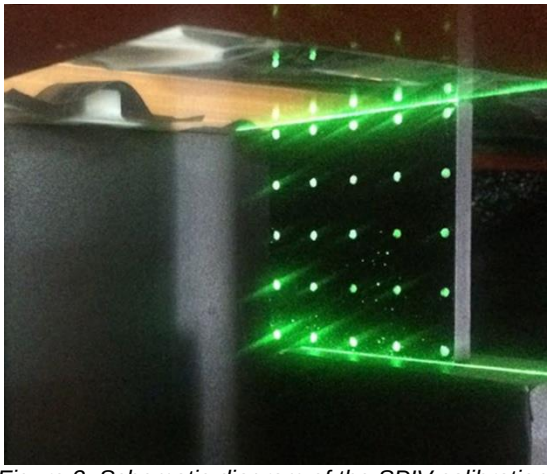

Figure 3: Schematic diagram of the SPIV calibration

Choice of SPIV Configuration

The conventional two-dimensional PIV measurement system can only obtain the results of the two-dimensional velocity in the measured section, and cannot obtain the third velocity component of the normal direction of the measured section. Therefore, this is called 2D-2C PIV measurement, as shown in Fig. 4(a). The 3D PIV measurement is based on the 2D-2C PIV and uses the basic principle of biological vision similar to that in the natural world. Two digital CCD cameras are used to photograph the experimental area. The two cameras are spatially arranged at a certain tilted angle. Two sets of two-dimensional velocity vector fields are obtained, and then the third velocity component in the experimental region is obtained by synthesis calculation. This method is customarily referred to as 2D-3C PIV measurement, and Fig. 4(b) and Fig. 4 (c) show a three-dimensional PIV schematic diagram.

For 3D PIV measurement, the camera and laser plane in the 3D system have a certain angle. In order to make the captured image clear, the camera chip plane, the lens plane and the captured image plane must meet the Scheimpflug optical conditions (the extended plane of laser plane, lens plane, and camera chip plane is intersected by a line. This ensures that the measurement results are not only safe, and also reliable and accurate.

This paper focuses on the flow characteristics of the flow along the channel in the tip region, and at the same time, it can obtain more instantaneous flow field information in the blade channel. Therefore, the PIV test scheme of 2D-3C PIV layout 2 in Fig. 4(c) is applied.

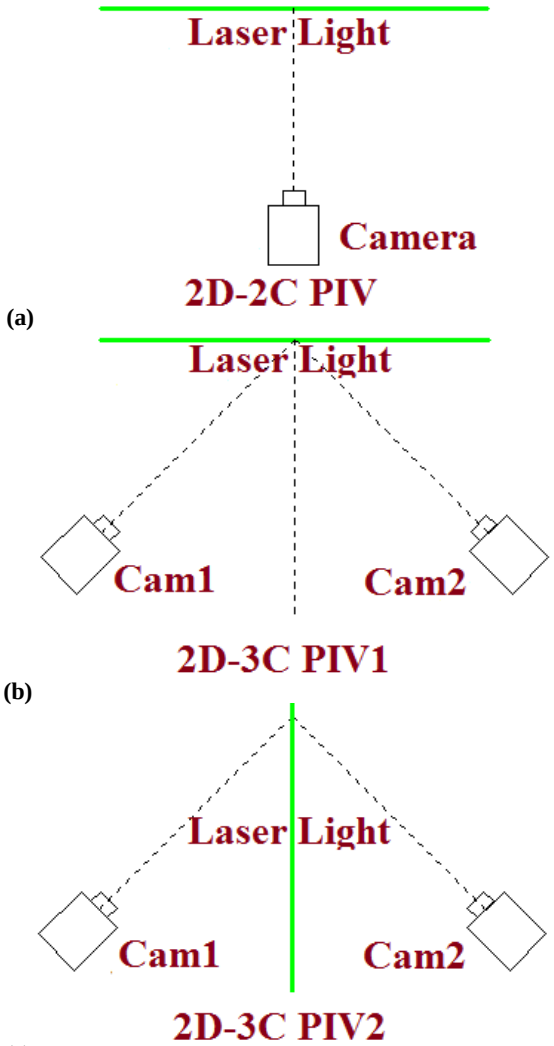

Figure 4: Schematic diagram of PIV configuration

Schematic Layout of Measured Planes

The layout of the SPIV experimental test scheme is shown in Fig. 5. The measurement sections in the channel starts from 20% of the camber line to 110% camber line, which is shot once every 10% of the camber line. And the measurement section is perpendicular to the local tangent line of camber line. The specific scheme layout is shown in Fig. 5. Due to the large degree of curvature of the turbine blades, the space position of the camera, laser displacement mechanism, etc. needs to be changed every time with the measurement cross-section is changed during the experiment. This will not only be time-consuming, but also leads to a large measurement error.

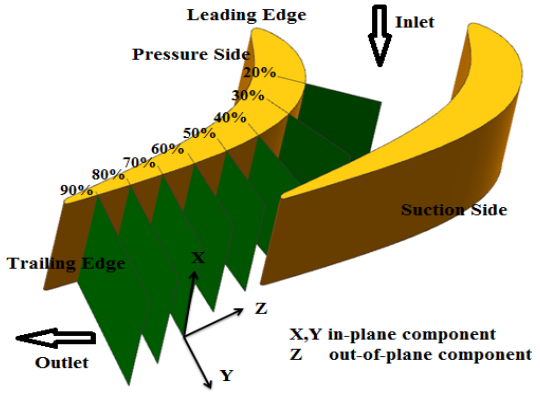

Figure 5: Schematic layout of measured planes

Image Acquisition and Data Processing

The image calculation uses a cross-correlation algorithm, the number of iterations is 1, the query area window size and iterative step size are 32×32 pixels and 16×16 pixels respectively, and the GPU acceleration calculation is used during the image calculation process.

The images were obtained inside the passage between the second blade and third blade, as can be seen in Figs. 1 and 2. In every measured plane, 400 instantaneous images are acquired. The inter-frame time, dt, is set as 10 μs based on a nearly 10 m/s maximum flow velocity at inlet of linear turbine cascade and yields a maximum particle-image displacement less than 8 pixels. The MicroVec V3 and in-house procedure are applied to the post-processing of SPIV. During the data processing, the interrogation window and step size are set to 32pixel×32pixel and 12pixel×12pixel respectively. The grid spatial resolutions of the velocity vector are about 0.39309mm. As known in references [13], the strong peak locking often appeared. In this study, some methods were employed to relieve the effect of peak locking. The histogram of the measured particle-image displacement at 50% camber line cross section, showed in Fig.5, demonstrates that the peak locking behavior is successfully controlled.

MEASUREMENT ACCURACY

In general, SPIV measurement technique has a wide range of measurement accuracy factors. In summary, it mainly includes the following six aspects: a) random error of image noise; b) image shift error; c) particle follow-up error; d) particle acceleration Error; e) particle velocity gradient error; f) image calibration error, each influencing factor is not independent, but in order to make an assessment of measured results, it is divided into random error and systematic error for discussion and analysis. Among them, random errors are often referred to as Type A errors and system errors are referred to as Type B errors.

According to the principle of PIV, the accuracy of PIV testing is mainly determined by the center position of the tracer particles [17][18][19]. However, the results of the research show that when the diameter of the image particle is less than 1 pixel, the pixel value that is likely to be displaced by the conventional image algorithm tends to concentrate on the integral multiple of the pixel. This phenomenon is called the Peak Locking phenomenon [20]. The result is that the particle displacement accuracy is only 0.5 pixels, resulting in a large error. In order to eliminate the peak-locking phenomenon, the following methods are commonly used: 1) searching for the center position of the tracer using a Gaussian fitting sub-pixel fitting method; 2) increasing the magnification of the shooting lens, which can be achieved using a macro lens; 3) Increasing the diameter of the particle image appropriately. Fig. 6 shows the distribution of particle image displacement vectors at 90% of the camber line. It can be seen from the figure that the peak-locking phenomenon is effectively controlled in this experiment.

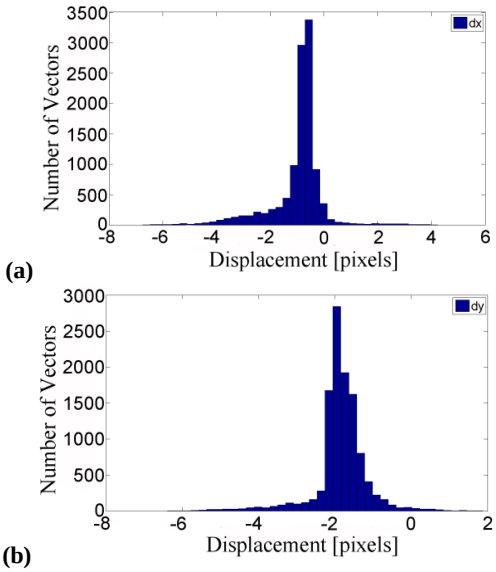

Figure 6: Peak locking (a) tangential velocity component, (b) radial velocity component

Fig. 7 shows the transient velocity contour and the statistical averaged velocity contour at 90% measured section. It can be clearly seen from the diagram that the velocity at the tip vortex core region is smaller and farther from the leakage region. Mainstream velocity is higher, and the effects of leakage flow/vortex are weaker.

Fig. 8 shows the relative uncertainty contour of transient velocity and vorticity at 90% measured section. As can be seen from the figure, the area, where the transient velocity is relatively uncertain, is located in the central area of the leakage flow. The closer to the center of the vortex core, the greater the uncertainty, the center of the vortex core reaches 5%, the periphery of the leakage area reaches 2.4%, and the area far from the leakage

flow area is less than 0.8%. For the transient vorticity uncertainty, due to the mainstream, the regional velocities are larger and the vorticity is smaller. The relative uncertainty of vorticity in the main part of the region reaches 10% to 20%. The leakage area is the location where the vorticity is relatively large, and the relative vorticity uncertainty is relatively low. Basically, the vorticity is below 2%.

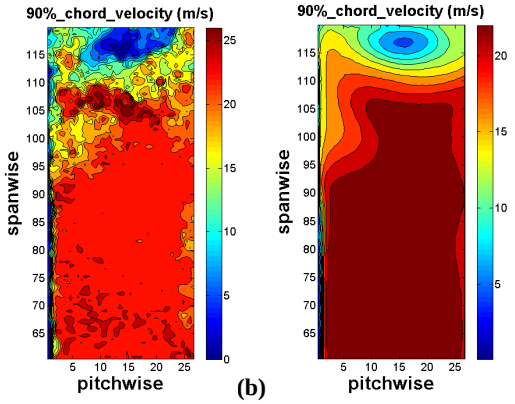

Figure 7: Velocity contour at 90% measured plane (a) instantaneous velocity, (b) time-averaged velocity

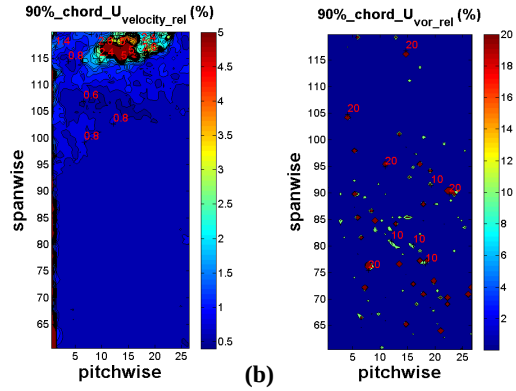

Figure 8: Measurement accuracy of instantaneous flow field (a) relative measurement accuracy of velocity, (b) relative measurement accuracy of vorticity

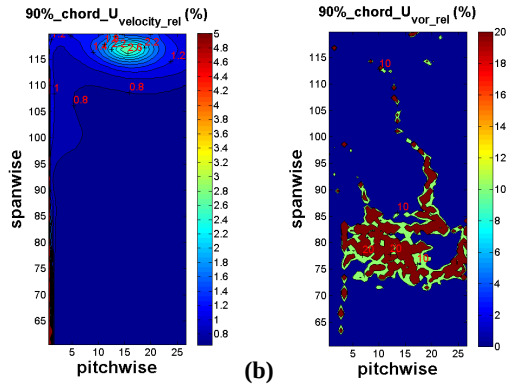

Figure 9: Measurement accuracy of time-averaged flow field (a) relative measurement accuracy of velocity, (b) relative measurement accuracy of vorticity

Figure 9 shows the relative uncertainty contour of combined velocity and vorticity for a statistical averaged flow field at 90% measured section. The relative uncertainty distribution of the statistical averaged flow field is similar to that of the transient flow field. However, the relative uncertainty of the statistical averaged flow field is calculated by taking into account the random error (Type A) and the systematic error (Type B). Therefore, the relative uncertainty distribution contour of vorticity can clearly show that the area with larger uncertainty in the mainstream area increases sharply and the uncertainty value of vorticity also increases.

RESULTS AND DISCUSSIONS

Analysis of convergence characteristics

Concerning the convergence problem encountered in the post-processing calculation of image data, this paper makes a simple analysis. As shown in Fig. 10, the convergence results of the flow field in the upper half of the outlet section. This can be used to derive convergence criteria for the PIV measurement of this turbine cascade experiment. As can be seen from the figure, 300 valid sampling numbers can satisfy the convergence of statistics such as velocity and vorticity in the mainstream area of the channel. In the tip region, approximately 400 valid sampling numbers can also satisfy the statistics. After comprehensive consideration, it is determined that the number of samples in the SPIV data processing calculation is 400.

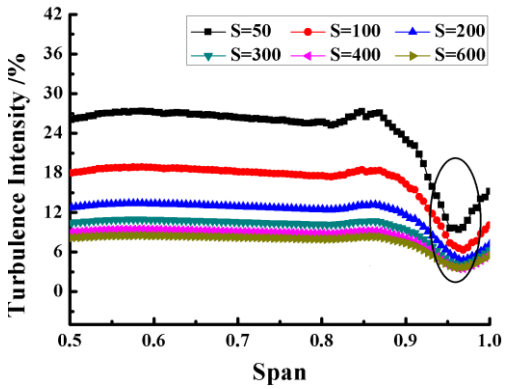

Figure 10: Determination of convergence characteristics of measurement results for Cascade outlet sections

Instantaneous and time-averaged flow fields

Figs. 11 and 12 show the identification results of vortex core at 40% and 90% of the measured cross section at different instants in the reference tip clearance. It can be seen from Figs. 11 and 12 that the leakage flow in the tip region is not just a single vortex structure but a concentrated vortex structure composed of many vortices, and the scale

and intensity of the vortices vary from one vortex to another. However, all the vortexes in the tip leakage area are located in the left half of the channel, and the performance is more concentrated in 40% of the measured section. From the foregoing, it can be seen that it corresponds to the area with the strongest leakage. When the leakage vortex splits into small vortices, and the blending with the mainstream increases, each tiny vortex floods the entire tip channel, and the range of motion migrates toward the root, as shown in Figure 12. The shape and size of the vortex vary greatly at different times and have randomness, which indirectly explains the unsteady characteristics of the leakage flow/vortex in the tip region.

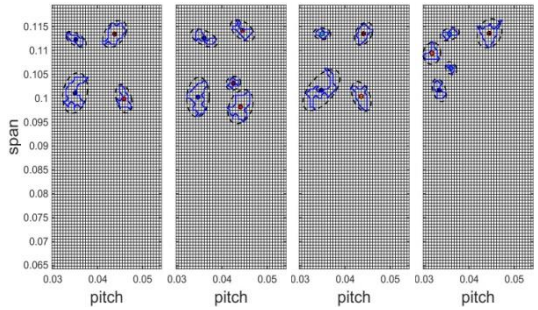

Figure 11: Transient flow field at 40% measured plane

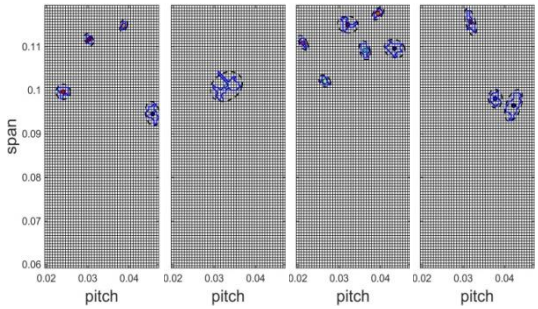

Figure 12: Transient flow field at 90% measured plane

Figs.13 and 14 present the combined contours of streamwise velocity and vorticity inside the turbine cascade passage. As shown in Fig.14, the tip leakage flow appears at the position of 30% camber line. But the tip leakage flow is not very intense at this time, because a very small amount of flows is involved in the mainstream, which is caused by the low pressure gradient of pressure side and suction side. When the flow propagates downstream and passes by the measured plane of 40% camber line, the pressure difference increases and promotes the formation of leakage flow. Consequently, the tip leakage vortex with high vorticity appears the suction side and affects the flows near the suction side of the blade. As the flow spreads downstream, more and more flows pass by the tip clearance gap and rolls into the main stream, which finally enhances the tip leakage flow/vortex. As shown in the flow field of measured plane of 50% camber line, the region of the leakage region expands and the intensity of leakage flow also increases the most. When the flow continues to move, the tip leakage vortex becomes a little weak, which can lead to the vortex being unstable. The reason for this result is that the tip leakage vortex has an interaction with mainstream. However, there is no enough leakage flow keeping the tip leakage vortex moving. As shown in Fig. 13, it has this trend in the measured plane of 60% camber line. At 70% camber line, the low pressure difference leads to the weak tip leakage flow. Therefore, the tip vortex core expands tangentially and changes into an elliptical shape. This is an indication of the breakdown of tip leakage vortex. Due to the interaction of the tip leakage flow and main stream, the tip leakage vortex gradually dissipates and the low momentum flow fills up the tip region.

Figs.15 and 16 show the combined contours of the turbulence intensity and kinetic energy. As shown, it can be seen that the turbulence intensity along the trajectory of the tip leakage vortex is highest except for the measured planes of 80% and 90% camber line where the high intensity of turbulence moves away from the suction side. This is caused by the wake of adjacent blade. In the turbine passage, the leakage flow propagates being close to the suction side of blade because of the favorable pressure gradient. However, the turbulence intensity in tip region reduces fast after the tip leakage vortex breaking down, which is owing to the adequate mixing of the leakage flow and mainstream as well.

The developments of turbulence intensity and turbulent kinetic energy are pretty similar. It reaches the maximum at the middle position of the blade passage. Since the blades are relatively flat, the tip leakage flow intensity is weak, and the turbulence intensity and turbulence energy are weakened. However, the area of the high turbulent area has increased.

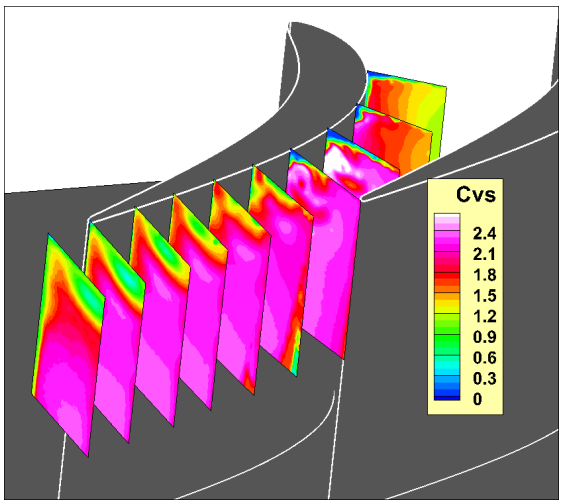

Figure 13: Combined maps of streamwise velocity

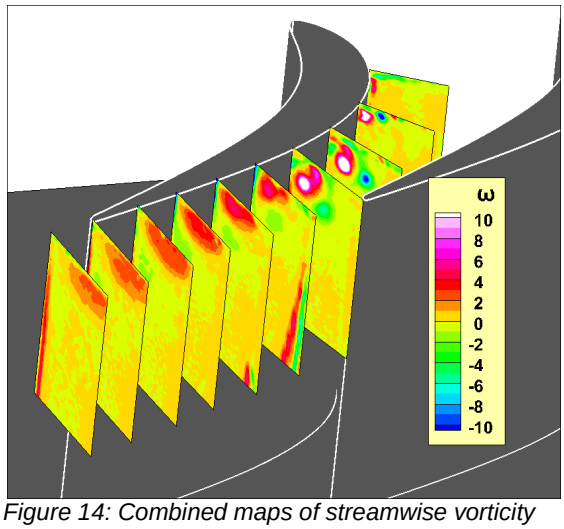

Figure 14: Combined maps of streamwise vorticity

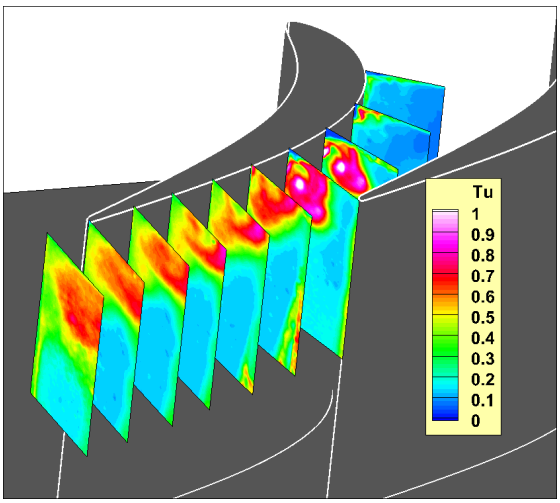

Figure 15: Combined maps of turbulence intensity

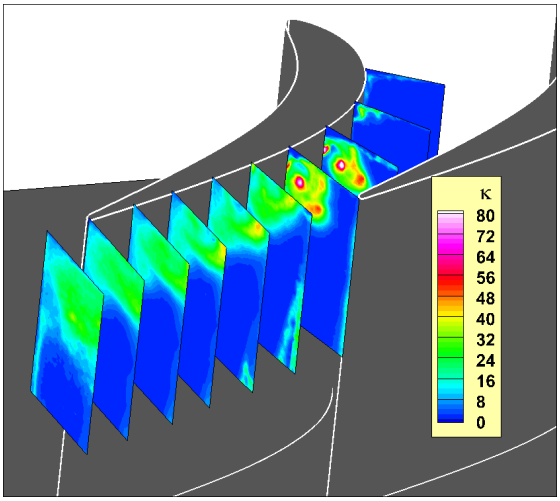

Figure 16: Combined maps of kinetic energy

Statistics flow fields

As shown in Fig. 17, the statistical average flow field based on Lambda2 vortex identification in the 40% and 90% measured sections is given, and the identified vortex core boundary is elliptically fitted. As shown in the figures, the blue line represents the boundary of the identified vortex core, the black dotted line represents the fitted ellipse, and the center of the ellipse is represented by a red pentagram. The figure on the graph indicates the vortex ring volume at the current position. Since the statistical average erases some of the tiny results in the transient flow field, it can be seen from the above illustrations that the identified vorticity is relatively weak.

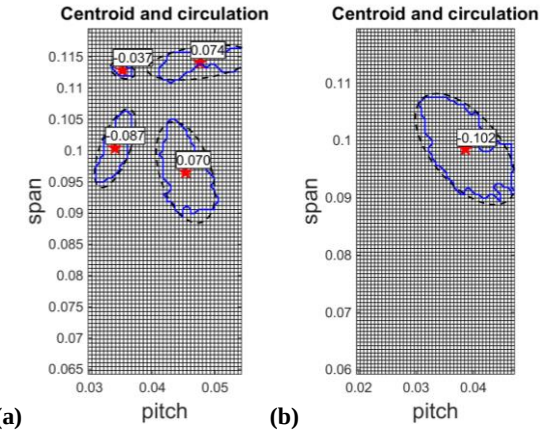

Figure 17: Statistical averaged flow field (a) 40% measured plane, (b) 90% measured plane

CONCLUSIONS

In this investigation, the SPIV measurements with the configuration that the CCD cameras were placed at different sides of the laser light sheet were used to investigate the flow fields inside the turbine passage. Some specific flow features inside the passage, such as the TLV evolution, TLV breakdown, and turbulence characteristics, can be obtained.

The intersection angle of the CCD cameras is a critical parameter for the balance of errors of the in-plane and out-of-plane components. In the actual experiment process, the angle between the two camera axes is 90°.

The measured results of the PIV experiments are largely determined by the properties of the tracer particles. In the linear turbine cascade, the spraying position of the tracer particles could be located at the upstream of the expansion section of the wind tunnel.

Detailed analyses of the measurement accuracy are also made in this study. Peak locking effect is effectively controlled. The velocity error of the mainstream area does not exceed 1%, and the measurement error of the leakage area does not exceed 3%. The statistical vorticity can meet the requirements of flow field analysis.

The measured results can successfully reveal the development and evolution of the tip leakage vortex/flow.

ACKNOWLEDGMENTS

This project was supported by Science and Technology Foundation of State Key Laboratory (Grant No. 9140C410205130C41153). And it was also funded by the National Natural Science Foundation of China, Grant No. 51161130525 and 51136003, supported by the 111 Project, No. B07009.

REFERENCES

[1] Horlock, J. H.; Lakshminarayana, B.; 1973. "Secondary flows: theory, experiment, and application in turbomachinery aerodynamics". Ann Rev Fluid Mech. 1973, 5:247 – 280

[2] Hunter, I. H.; Cumpsty, N. A.; 1982. "Casing wall boundary layer development through an isolated compressor rotor". J Eng Power. 104:805 – 818

[3] Lakshminarayana, B.; Murthy, K. N. S.; 1987. "Laser Doppler Velocimeter measurement of annulus wall boundary layer development in a compressor rotor". ASME paper, 87-GT-251

[4] Suder, K. L.; Celestina, M. L.; 1994. "Experimental and computational investigation of the tip clearance flow in a transonic axial compressor rotor". ASME Paper, 94-GT-365

[5] Ma, H. W.; Jiang, H. K.; 2000. "Three-dimensional turbulent flow of the tip leakage vortex in an axial compressor rotor passage". ASME paper, 2000-GT-503

[6] Miller, R. J.; Moss, R. W.; Ainsworth, R. W.; Harvey, N . W.; 2003. "Wake, shock, and potential field interactions in a 1.5 stage turbine-part I: vane-rotor and rotor-vane interaction". ASME J Turbomach. , 125:33 – 39

[7] Bryanston-Cross, P. J.; Towers, C. E.; Judge, T. R. et al.; 1991. "The Application of Particle Image Velocimetry (PIV) in a Short Duration Transonic Annular Turbine Cascade". Asme Transactions Journal of Turbomachinery, 114(3):504-509.

[8] Wernet, M. P.; 1997. "PIV for turbomachinery applications". Proceedings of SPIE - The International Society for Optical Engineering, 3172:2-16.

[9] Ni, B.; Xu, J.; Xue, R. et al.; 1998. "Quantitative Measurement and Visualization of Flow around Plate Cascade Using PIV". Journal of Ship Mechanics, vol.2, (3): 1-5.

[10] Lang, H.; Mørck, T.; Woisetschläger, J.; 2002. "Stereoscopic Particle Image Velocimetry in a Transonic Turbine Stage". Experiments in Fluids, 32(6):700-709.

[11] Wernet, M. P.; Zante, D. V.; Strazisar, T. J. et al.; 2001. "Characterization of the Tip Clearance Flow in an Axial Compressor Using 3-D Digital PIV". Experiments in Fluids, 39(4):743-753.

[12] Ma, H. et al.; 2015. "Experimental investigation of effects of suction-side squealer tip geometry on the flow field in a large-scale axial compressor using SPIV". Journal of Thermal Science, 24(4):303-312.

[13] Yu, X. J.; Liu, B. J.; 2007. "Stereoscopic PIV Measurement of Un-steady Flows in an Axial Compressor Stage". Experimental Thermal & Fluid Science, 31(8):1049-1060.

[14] Ma, H. and Wang, L.; 2015: "Experimental study of effects of tip geometry on the flow field in a turbine cascade passage". Journal of Thermal Science, 24(1):1-9.

[15] Willert, C.; 1997. "Stereoscopic Particle Image Velocimetry for Application in Wind Tunnel Flows". Meas. Sci. Technol. , 8: 1465-1479.

[16] Prasad, A. K.; 2000. "Stereoscopic Particle Image Velocimetry". Exp. Fluid, 29:103-116.

[17] Raffel, M.; Willert, C.; Kompenhans, J.; 2007. "Particle image velocimetry: a practical guide[M]". 2th ed., Berlin: Springer Verlag.

[18] Boillot, A.; Prasad, A. K.; 1996. "Optimization procedure for pulse separation in cross-correlation piv[J]". Exp Fluids, V21(1): p. 87-93.

[19] Westerweel, J.; 2000. "Theoretical analysis of the measurement precision in particle image velocimetry[J]". Exp Fluids, VSuppl: p. S3-S12.

[20] Westerweel, J.; 1997. "Fundamentals of digital particle image velocimetry[J]". Measment Science and Technology, V8: p. 1379-1392.